A Comparative study on the impact of urbanisation on microclimate in Cairo (Egypt) and London (UK) using remote sensing and Machine Learning

Lara Sabobeh[1], Tarig Ali[2], Maruf Md. Mortula[3]

[1]Department of Civil Engineering, American University of Sharjah, Sharjah P.O. Box 26666, United Arab Emirates - lara.sabobeh@outlook.com
[2]Department of Civil Engineering, American University of Sharjah, Sharjah P.O. Box 26666, United Arab Emirates - atarig@aus.edu
[3]Department of Civil Engineering, American University of Sharjah, Sharjah P.O. Box 26666, United Arab Emirates - mmortula@aus.edu

Keywords: Remote Sensing, Machine Learning, LULC Classification, Climate Change, GEE, Urban Heat Island.

Abstract

Urbanization significantly affects local microclimates, contributing to the urban heat island (UHI) effect, particularly in rapidly expanding cities. Effective monitoring of these changes is crucial for sustainable urban planning and climate adaptation. This study presents a comparative analysis of the impact of urbanization on the microclimates of two large, socio-economically distinct cities—Cairo, Egypt, and London, UK—between 2000 and 2023. Cairo's rapid, unplanned urban expansion contrasts with London's more regulated, gradual growth, providing an opportunity to assess how different urbanization patterns and climates influence UHI effects. Using Landsat Collection 2 satellite imagery and Google Earth Engine (GEE) for classification, Land Use and Land Cover (LULC) was divided into four categories: water bodies, vegetation, developed areas, and barren land. Several machine learning (ML) algorithms were compared, with Support Vector Machine (SVM) ultimately selected for its superior performance. The classified data were further analysed in ArcGIS Pro. The results show a 45% increase in developed land and a 38% reduction in vegetation in Cairo, leading to an average LST increase of 5°C. London experienced a 25% increase in developed areas and a 20% reduction in green spaces, with LST rising by 2.5°C. The study achieved an overall classification accuracy of 0.89 and a kappa coefficient of 0.85, demonstrating the effectiveness of SVM across both cities with differing climates. This research contributes to urban sustainability efforts by identifying the best ML approach for monitoring LULC changes in distinct global cities, offering insights for data-driven urban planning and UHI mitigation.

1. Introduction

Urbanisation is one of the defining trends of the 21st century. Currently, over half of the global population lives in urban cities, which is more than double the urban population in 1950 and is expected to reach 68% by 2050. The United Nations World Cities Report projects that this population growth will cause a 141% increase in city land area in low-income countries, which is significantly higher than the land increase in upper-income countries of 13% (Anonymous 2018). Rapid urban development has caused a loss in vegetation and wetlands, resulting in the degradation of ecosystems, which contributes to climate change, and eventual extreme weather phenomena (Bai, et al. 2018). The change in land use and land cover (LULC), particularly the replacement of vegetation cover and wetlands by impervious surfaces, is a major contributor to climate change, and unless serious actions are taken, the outcomes will have severe negative effects on the environment and wellbeing of people living in urban areas (Solomon 2023).

Continuous spatiotemporal monitoring of LULC changes caused by urbanization activities is crucial for the decision-making process related to the sustainable urban planning of cities. However, most of the data about urbanization's effects on the environment are collected by local governments and are not always available to the public. Remote sensing can provide key information to monitor rapid urbanization and help achieve sustainable development, using high- to mid-resolution remotely sensed images to provide a vital unbiased source of information for independent global environmental studies for LULC changes over the years (Gómez, et al. 2016; Solomon 2023). Traditional remote sensing classification methods have been foundational in creating LULC maps. Among the most prominent traditional methods are Maximum Likelihood Classification (MLC) and various kernel-based approaches. These methods typically rely on statistical and mathematical algorithms to classify image pixels based on their spectral signatures (Gómez, et al. 2016; Solomon 2023; Xu 2006). However, these methods have many limitations, as they often assume a normal distribution of the data, and sometimes they are unable to capture the complex interactions of the environmental features, making them inaccurate and ineffective in many cases.

To address these challenges, supervised machine learning offers a promising alternative for an effective LULC classification. Machine learning is a very effective approach for regression and classification of nonlinear systems. It’s especially useful when the theoretical knowledge of the system is incomplete, but sufficient observations of the system are available (Lary, et al. 2016). It’s ideal for complex multivariant systems. Image classification can be either supervised or unsupervised. Supervised classification relies on the pre-labeled training data set quantity and quality, while unsupervised classification uses clustering algorithms like K-means to group pixels with similar characteristics without the need for prior labelling (Wu, et al. 2019)(Lary, et al. 2016; Wu, et al. 2019).

Supervised machine learning classifiers can be very useful in LULC classification, especially if a good-quality and validated training data set is available. For example, Gradient Tree Boosting (GTB), Random Forest (RF), Support Vector Machine (SVM), and Classification And Regression Trees (CART), are among the most widely used supervised ML algorithms in LULC classification applications. However, most of the literature agrees that RF and SVM outperform other classifiers in most LULC classification scenarios due to their robustness and ability to

handle high-dimensional data effectively (Shih, et al. 2019). On the other hand, GTB, a relatively new algorithm (Ghayour, et al. 2021), showed a slightly better performance than the aforementioned classifiers in some studies (You, et al. 2022). However, no sufficient literature was found to compare it with other classifiers globally. CART, while simpler and faster to implement, often shows less robust performance compared to ensemble methods like RF and GTB, but still serves as a valuable tool for initial analysis and quick classification tasks. Further research is needed to fully understand the potential and limitations of GTB, compared to the other methods, in various LULC applications (Ahmed 2023).

However, generating high to mid-resolution (30 m) LULC maps on a large city, involves a huge amount of data and requires massive capabilities for storing, analyzing, and processing this data, which can take days to run a model and generate a single image, even if the highest-performance personal computers available were utilized. Google Earth Engine (GEE) is a freely available cloud-based platform that provides tools for remote sensing data processing and addresses the requirements for dealing with big datasets and allows for acquiring, processing, and comparing the resulting data with the massive datasets available on the platform, due to its high-performance and fast computing capabilities (Yang, et al. 2022).
To understand the environmental effects of urbanization and its impact on local climate change, key parameters like vegetation cover and the surface temperature (LST) should be considered. LST is widely affected by LULC changes (Gogoi, et al. 2019) as urban areas develop, and impervious surfaces increase, the LST increases as well. Many studies showed a clear positive correlation between LST and impervious surface density (urban area) and a negative correlation between LST and vegetation cover (Tran, et al. 2017). LST rise due to urbanization not only increases energy consumption during summer, contributing to global warming, it also accelerates the process of smog formation and air pollution (Arnfield 2003). LST can be estimated using satellite sensors with thermal bands that can detect thermal radiation from the earth’s surface.

Another important environmental factor that is affected by the change in LULC is the vegetation cover. Vegetation is a particularly important part of the earth’s ecosystem as it plays a vital role in the carbon and water cycle, and it is very sensitive to changes in temperatures. Normalized difference vegetation index (NDVI) is one of many indices used as a measure of the vegetation cover in remote sensing (Purevdorj, et al. 1998). The NDVI is one of the most widely used indexes in LULC classification, however, if used alongside other spectral indices such as the Normalized Difference Built-up Index (NDBI) and the Modified Normalized Difference Water Index (MNDWI), the LULC classification quality will increase especially that each of these indices is sensitive to different types of land cover (Pareeth, et al. 2019). The traditional approaches for LULC classification such as the Maximum Likelihood use suitable thresholds of the indices for each class type and assume normally distributed classes with linearly separable relationships, which is not true for most of the cases (Chen, et al. 2006). However, the use of supervised machine learning algorithms allows for accurate and effective LULC classification and captures the non-linear and complex relationships within the data, without the need for accurate pre-defined thresholds, depending on the quality of training data (Qu, et al. 2021).

This research compares the impact of LULC changes on local climate in two major global cities in the 21st century, Cairo and London, specifically in 2000, 2010, 2020, and 2023. Moreover, LULC layers over the period of study were created through supervised classification using four machine learning algorithms. The impact of LULC changes on local climate was then studied by examining the relationships between LULC and the corresponding LST layers over the period of study. The novelty of this research is that it explores the new GTB method and compares it to other well-established methods, using advanced accuracy metrics, and grid-based hyperparameter tuning.

2. Study Area

This study focuses on two large cities: Cairo, Egypt, and London, UK. These cities were selected for their distinct socio-economic contexts, climatic zones, and contrasting patterns of urbanization, providing a valuable comparative framework to assess the effects of urbanization on microclimates and the urban heat island (UHI) effect.

2.1 Cairo, Egypt

Cairo, the capital of Egypt, is located at approximately 30.0444° N latitude and 31.2357° E longitude south of the Mediterranean. It lies within a hot desert climate zone, characterised by extremely hot summers and mild winters, with minimal rainfall throughout the year. The Nile River runs through the Cairo metropolitan area, known as Greater Cairo, the largest metropolitan area in Africa. Greater Cairo covers an area of about 2217.71 km² across three governorates: Cairo, Giza, and Qalyubia. Its population has experienced rapid growth, reaching approximately 20.57 million in 2020, with an average growth rate of 50.9% between 2000 and 2020. This rapid population increase has fuelled significant, often unregulated, urban expansion, leading to a notable loss of vegetation, particularly along the Nile’s shores. The city's Gross Domestic Product (GDP) is estimated at $105 billion, contributing approximately 22% of Egypt’s overall GDP, underscoring its importance as the developing nation's economic and political hub.

Since the 1960s, Cairo’s population has expanded largely in an unplanned manner, with high-density developments replacing natural land cover, exacerbating the urban heat island (UHI) effect. These informal developments, or slums, accommodate about 63% of Greater Cairo’s population, who suffer from insufficient infrastructure, and generally poor socioeconomics (Kipper, et al. 2009) . This study investigates the impact of these rapid urban changes on local climate, focusing on the increase in Land Surface Temperature (LST) due to urbanization. The study area covers Greater Cairo, based on the latest administrative boundaries reported by the Egyptian government. Figure 1 illustrates the extent of Greater Cairo examined in this study.

This contribution has been peer-reviewed. The double-blind peer-review was conducted on the basis of the full paper.
https://doi.org/10.5194/isprs-annals-X-G-2025-737-2025 | © Author(s) 2025. CC BY 4.0 License.

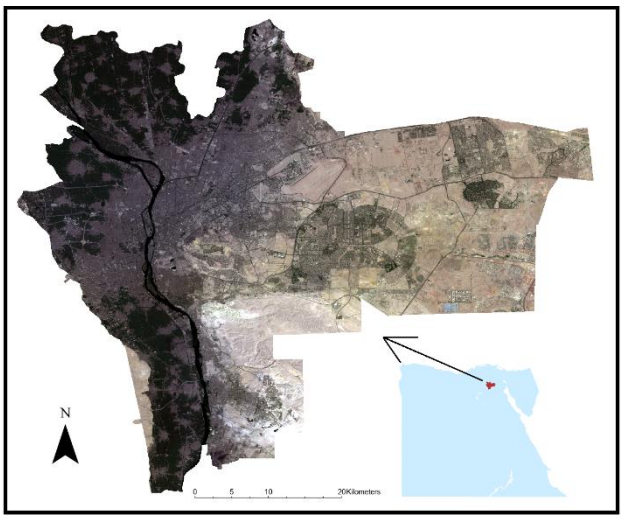

Figure 1. Map of the study area (Greater Cairo).

2.2 London, UK

London, the capital of the United Kingdom, is located at 51.5074° N latitude and 0.1278° W longitude, within the temperate maritime climate zone. Covering an area of 1594 km², the city lies along the Thames River, which has shaped its urban layout and green spaces. By 2020, London’s population reached 9.3 million, with a growth rate of around 18% from 2000 to 2020. London’s GDP, estimated at $565 billion, further cements its status as a global financial hub. Unlike cities experiencing rapid, unregulated growth such as Cairo, London’s urban expansion has been more carefully managed. Strict planning regulations aim to protect green spaces and limit unchecked development, particularly in suburban and former industrial areas.

Over the past 50 years, London has experienced significant LULC changes. The city has transitioned from primarily industrial land use to a blend of high-density residential, commercial, and mixed-use developments. Suburban areas have expanded into what was once agricultural land, transforming into residential neighbourhoods (Rowland, et al. 2020). Despite the urban growth, London has managed to preserve and even expand its green areas. However, the reduction in natural land cover in newly developed areas has contributed to rising local temperatures, intensifying the UHI effect. This study examines the relationship between regulated urbanisation and local climate impacts, specifically rising LST, and contrasts these trends with Cairo’s more rapid, unregulated urban growth and more extreme UHI effects. Figure 2 shows the Greater London area, consisting of different wards, chosen as the focus of this study.

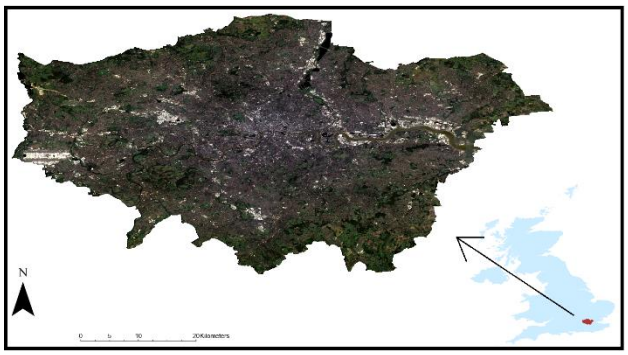

Figure 2. Map of the study area (Greater London)

3. Data and Methods

3.1 Dataset

Landsat Collection 2 images were acquired and used in this study to create annual composites for 2000, 2010, 2020, and 2023. Landsat Collection 2 images were selected for different reasons. Firstly, their medium resolution (30m) is optimal for an environmental study on a large city scale, as it is high enough to capture the important parameters and not too high that processing time is not practical. Secondly, they are the longest-running satellites that have captured remotely sensed imagery of the Earth since 1972, so the results of this study can be used for future work that uses the same dataset. Thirdly, they are freely available in GEE and provide consistent global coverage. Landsat satellites overlap in their operation years, for example, Landsat 5 TM and Landsat 7 ETM+ both cover the years 2000 and 2010. In other words, each location on Earth is captured by more than one satellite sensor at any time after 1982. Additionally, each Landsat satellite captures images of the same area almost every 16 days (return period). To capture as much data as possible from each scene, all images from Landsat satellites operating during the period from 2000 to 2023 will be combined into one image collection. Collection 2 surface reflectance Tier 1 data were used because they provide atmospherically corrected surface reflectance and land surface temperature with higher radiometric and positional accuracy than Tier 2 data. Figure 3 below illustrates the workflow followed to generate the LULC and the LST maps. A detailed explanation of the steps can be found in the subsequent sections.

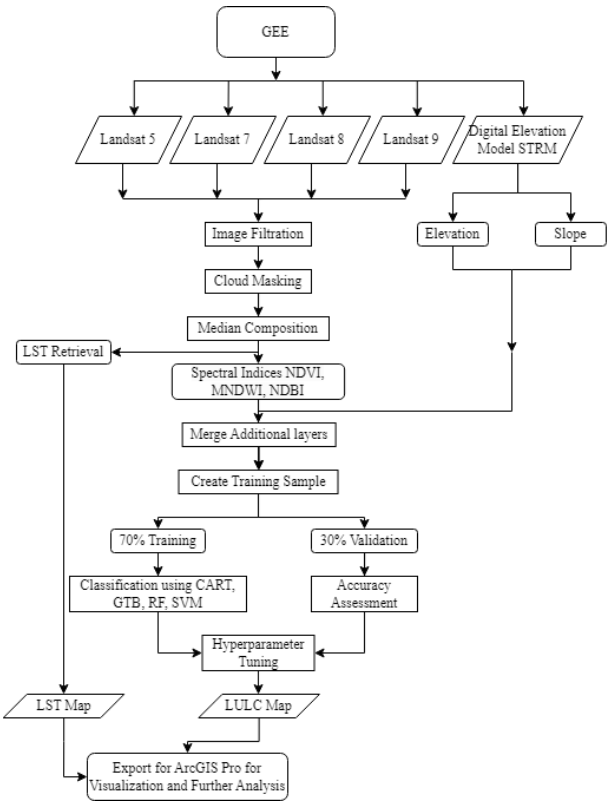

Figure 3. Methodology flowchart.

3.1.1 Data Preprocessing: After importing the Landsat 5-9 image collections into Google Earth Engine (GEE), the "QA_PIXEL" band was used to identify and mask out pixels affected by clouds, shadows, or snow, as detected by the CFMask algorithm. The "QA_RADSAT" band was then applied to remove saturated pixels that were unusable. This process produced a cloud- and shadow-free image collection with no saturated pixels. The integer digital number (DN) values of the bands were then rescaled to their original floating-point values using the appropriate scaling factors and offsets. All image collections were merged into one large collection to get as much data as possible for each location. The collection was clipped to the study area to speed up processing and filtered to ensure coverage of the entire study period, which was the whole 12 months of each study year. Each location had a maximum of 24 images per year, representing two monthly captures, from at least one satellite at a time. To create a single image for each location, the median function was used, which assigned the median pixel value across all images. Initially, the study focused on images from May to September, but gaps in the 2000 and 2010 images required expanding the study period to 12 months. This filled gaps and improved image quality. In 2010, data gaps from the Landsat ETM+ sensor failure were interpolated using surrounding pixels, enhancing image continuity.

3.1.2 Training And Validation Sample Collection: After importing, preprocessing, and filtering the data, collecting the training samples LULC classification is the next step, into four general LULC classes: Water bodies, vegetation areas, developed areas, and barren land. There is no strict limit on sample size, but larger samples generally improve accuracy. However, manually collecting samples is time-consuming, and larger datasets increase processing costs in GEE. Therefore, a balanced sample size is important. In this study, at least 40 samples per LULC class were manually and randomly collected for each city from cloud-free Landsat images for 2000, 2010, 2020, and 2023. These points were selected to cover variations within each class, ensuring a balanced and accurate dataset. The resulting feature collection was exported and re-imported as an asset to reduce processing time. The dataset was then overlaid on training images and split into 70% for training and 30% for validation. Table 1 summarizes the collected sample and distribution.

Year	Class				Training Sample	Validation Sample
	Water	Vegetation	Developed	Barren		
2000	90	92	90	90	253	109
2010	91	89	92	91	254	109
2020	90	90	92	91	254	109
2023	92	91	89	91	254	109
Sum	**363**	**362**	**363**	**363**	**1015**	**436**

Table 1. Collected data description.

3.1.3 Additional Layers Calculation: To improve the models' accuracy, additional indices and auxiliary data were calculated, and combined with the median image. These incidences are the normalized difference vegetation index (NDVI), the normalized difference-built index (NDBI), and the modified normalized difference water index (MNDWI). Topographical features (Slope and Elevation) were captured using the Digital Elevation Model (DEM) from the Shuttle Radar Topography Mission (SRTM) [101] because of its global coverage, and accuracy, and the pixel size is 30 m, which is the same as the pixel size of other data. This resulted in creating 3 index bands, and 2 topography bands, in addition to the 6 original spectral bands from the satellite sensors. These 11 bands were combined to create one image for each year of the study. Landsat 4-9 collection 2- Level 2 products contain a ready-to-use Surface Temperature band, in Kelvin as a 30 m grid. Therefore, this research simply converted these from Kelvin to degrees Celsius °C.

3.2 Supervised Classification

GEE was used to perform supervised classification, utilizing training image bands and training samples collected in the previous steps. The 11 bands (features) retrieved in the earlier steps were normalized based on the minimum and maximum values of each band to enhance the performance of the classifiers. After that, the CART, GTB, RF, and SVM classification models, which are readily available in GEE, were applied to the normalized image in GEE using the training sample. However, the performance of these models is highly dependent on the values chosen for the hyperparameters for each model. Therefore, grid-based hyperparameter tuning trials were performed for each model at least 200 times, by training and testing the model for every hyperparameter value in a series of possible values, against other series of values for other parameters. After hyperparameter tuning, the optimal parameter that maximized validation accuracy while keeping overfitting below 3% was selected. Table 2 below shows the hyperparameters’ values that were finally used for training the models.

Model	Hyperparameter	Value
CART	maxNodes	10
	minLeafPopulation	32
GTB	maxNodes	70
	numOfTrees	30
RF	numOfTrees	70
	minLeafPopulation	12
SVM	Cost	1024
	Gamma	0.0078125

Table 2. Optimal hyperparameters values used.

Classified images initially showed a "salt and pepper" effect due to misclassification noise, which was resolved using Simple Non-Iterative Clustering (SINC) for image segmentation. This unsupervised clustering technique replaced misclassified pixels with the majority cluster value using GEE. However, due to data volume, further analysis was conducted in ArcGIS Pro instead.

For accuracy assessment, the data was split into 70% for training and 30% for validation, with confusion matrices and metrics calculated in GEE. Key metrics included overall accuracy, producer’s accuracy (recall), consumer’s accuracy (precision), kappa statistic, F1-score, and the Z-score which compares classifier performance, with a Z-score above 1.96 indicating a 95% likelihood that one classifier performed better than another.

4. Results And Discussion

4.1 Classification Metrics Results

The study assessed four classifiers (CART, GTB, RF, and SVM) based on multiple accuracy metrics for LULC classification. SVM outperformed the others, achieving the highest validation overall accuracy (88.34%) and Kappa statistic (84.31%), indicating strong agreement between observed and predicted values. RF and GTB performed similarly, with RF having a slightly higher validation accuracy (86.2%) than GTB (86.04%). CART had the lowest performance, with a validation accuracy of 83.06%. Table 3 summarizes the results of the overall accuracy and Kappa statistics for both the training and validation samples.

Metric		CART	GTB	RF	SVM
Training Sample	overall accuracy	85.68	88.9	88.27	88.51
	Kappa Statistics	80.9	85.2	84.36	84.68
Validation Sample	Overall accuracy	83.06	86.04	86.2	88.34
	Kappa statistics	77.4	81.37	81.59	84.31

Table 3. Overall accuracy and Kappa statistics for the four models.

In terms of class-level accuracy, general trends showed that all models performed best in identifying the water class, while the developed and barren classes had the most variability in accuracy across the models. The F1-score, which is the harmonic mean of producer's and consumer's accuracy, was used to assess overall performance. SVM consistently outperformed the others, achieving the highest F1-scores across all classes. The water class had the highest F1-scores for all classifiers, while the barren class had the lowest. Figure 6 in the appendix summarizes the F1-score results.

Finally, the Z-score analysis indicated that SVM was superior to the other classifiers, with more than 84% confidence over CART, while RF and GTB performed almost equally. The Z-score results are summarized in Table 4. Z-score results.in the Appendix. Overall, SVM was the best model, followed by RF and GTB, with CART performing the worst.

4.2 LULC Maps

In comparing Cairo and London, the SVM model was used, as it performed better than the other models as discussed in the previous section, revealing key trends in land use and land cover (LULC) changes from 2000 to 2023. As shown in Figure 4, water bodies remained largely stable, with changes of less than 2% in both cities. However, vegetation cover steadily declined in both, reflecting the expansion of urban areas. The extent of this urbanisation differs between the two cities. Cairo saw a dramatic 90% increase in developed land, compared to a more moderate 58% increase in London. This suggests that Cairo is undergoing rapid urbanization, far outpacing London's growth. On the other hand, in Cairo, the barren area decreased from 54.04% in 2000 to 46.81% in 2023, still making up nearly half of the city's total land by the end of the study period. In contrast, London saw an increase in barren land, rising from 1.88% in 2000 to 9.95% in 2023. While Cairo continues to have the highest proportion of barren land, this decline suggests some conversion of barren land to other uses. This suggests that Cairo's expansion into undeveloped and barren land is more pronounced, while London's development likely focuses on previously developed or vegetated areas.

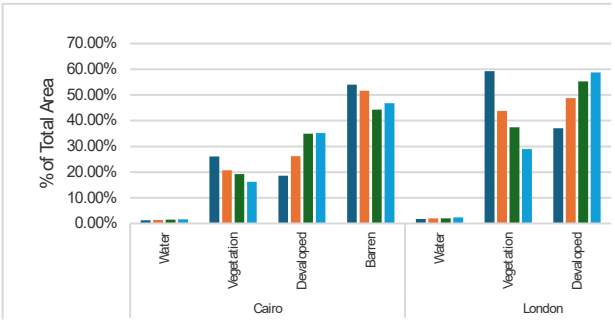

Figure 4. The percentage of area occupied by each of the classes in the two cities over the study period, based on the SVM model.

When comparing the LST in Cairo and London, both cities demonstrate clear impacts of urbanization on LST, reflecting the UHI effect. In Cairo, the mean LST rose from 36.35°C in 2000 to 39.92°C in 2023. London, with a lower overall LST, saw its mean temperature rise from 23.03°C in 2000 to 26.04°C in 2023. It’s also important to understand how different LULC patterns affect the LST. In both cities, water bodies consistently exhibit the lowest temperatures due to water’s high heat capacity, with temperatures around 30°C in Cairo and 18°C in London in 2023. Vegetation also helps regulate temperature, showing relatively cooler readings, especially in London, where vegetated areas had an LST of 20.33°C in 2023, compared to 35.55°C in Cairo.

However, developed and barren areas had the highest temperatures. In London, the developed areas had the warmest LST, rising to 26.81°C in 2023, highlighting the UHI effect. In contrast, Cairo's barren land, largely consisting of sand, was even warmer than developed areas. In 2023, barren land in Cairo reached a mean LST of 42.11°C, higher than the 39.51°C recorded in urban areas. This difference highlights Cairo’s unique thermal profile due to its hot, arid environment, where barren land absorbs and retains heat more effectively than urbanized areas. Overall, Cairo's LULC changes are characterized by extreme heat in barren areas, while London's developed regions contribute significantly to its UHI effect. Figure 5 shows the 2023 LST map (a) in comparison to the LULC map (b) for London. Figure 7 in the appendix shows the 2023 LST map (a) in comparison to the LULC map (b) for Cairo.

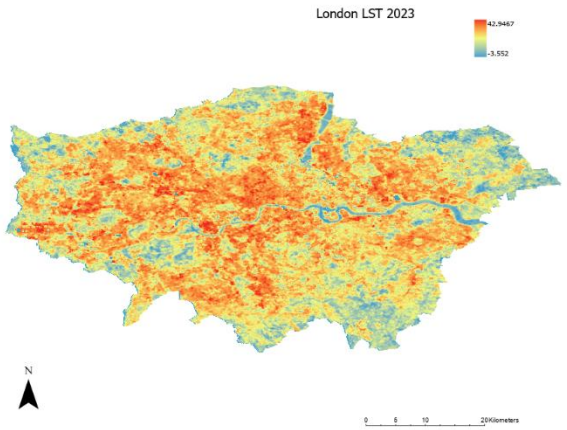

(a)

This contribution has been peer-reviewed. The double-blind peer-review was conducted on the basis of the full paper.
https://doi.org/10.5194/isprs-annals-X-G-2025-737-2025 | © Author(s) 2025. CC BY 4.0 License.

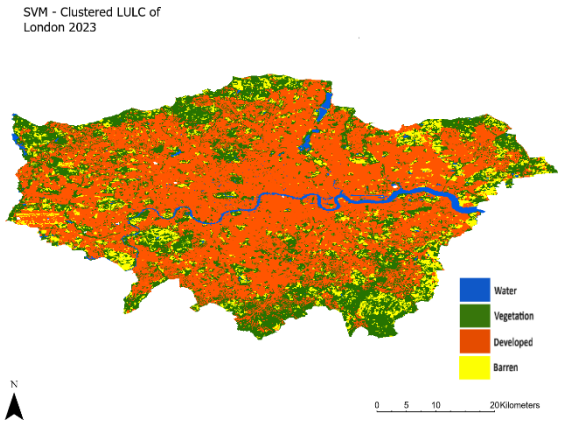

(b)

Figure 5. The 2023 LST map (a) in comparison to the LULC map (b) for London.

The comparison between Cairo and London over the study period reveals notable contrasts in urban development, vegetation loss, and land use intensity. Cairo’s vegetated area per capita decreased sharply by 59.36%, from 42.5 m² to 17.28 m², reflecting extensive urban expansion. London also saw a significant decline in vegetated area per capita by 61.82%, from 129.88 m² to 49.58 m², despite maintaining more green space than Cairo. Cairo’s Land Use Degree Index (LUDI), which measures the intensity of land use for human activities across different LULC classes, increased by 14.50%, from 1.65 to 1.88, driven by its urban growth. London’s LUDI rose more moderately, by 5.77%, from 2.35 to 2.49, indicating a slower increase in land use intensity. Both cities saw significant GDP growth, but London maintained much higher GDP per capita levels. These trends suggest Cairo is undergoing more rapid urbanization, with greater environmental strain, while London faces a more controlled but still impactful urban expansion.

5. Conclusion

This study conducted a comparative analysis of the impacts of urbanization on the microclimates of Cairo, Egypt, and London, UK, using remote sensing and machine learning techniques from 2000 to 2023. By GEE, large volumes of Landsat satellite imagery were effectively processed, demonstrating its capability to manage extensive datasets for environmental monitoring. The research highlights the effectiveness of machine learning algorithms in addressing complex environmental factors, particularly through the exploration of the new Gradient Tree Boosting (GTB) method. This study not only compares GTB with well-established methods like RF and SVM, but also employs advanced accuracy metrics and grid-based hyperparameter tuning to optimize model performance. Notably, SVM emerged as the most effective classifier, achieving an overall accuracy of 88.34% and a kappa coefficient of 0.84, indicating strong agreement between observed and predicted values. However, GTB also performed and was very similar to RF, which highlights its potential to be utilized in other studies.

Significant changes in LULC were observed, with Cairo experiencing a dramatic 89.6% increase in developed areas and a 37.66% decrease in vegetation, leading to a 3.5°C rise in LST. In contrast, London exhibited a 58.45% increase in developed land and a 51.04% reduction in green spaces, resulting in a more moderate LST increase of 3°C. These findings underscore the distinct urbanization patterns and their respective effects on microclimates in the two cities.

Future work should focus on expanding the geographical scope to include more cities with diverse urbanization trends. Additionally, integrating deep learning models could enhance classification accuracy and provide more comprehensive insights into LULC changes. Engaging local stakeholders to implement data-driven strategies for mitigating urban heat effects will also be vital for promoting sustainable urban development.

Acknowledgements

I would like to express my sincere gratitude to the American University of Sharjah (AUS) for providing the resources and support that made this research possible. I am especially grateful to my advisors, Dr. Tarig and Dr. Maruf, for their invaluable guidance, encouragement, and expertise throughout this work. Their insights and support have been instrumental in shaping this study.

References

World Urbanization Prospects: The 2018 Revision, Online Edition. 2018.

Ahmed, S.A., 2023. Land use and land cover classification using machine learning algorithms in google earth engine. Earth Science Informatics 16 (4), 3057–3073.

Arnfield, A.J., 2003. Two decades of urban climate research: a review of turbulence, exchanges of energy and water, and the urban heat island. International Journal of Climatology: a Journal of the Royal Meteorological Society 23 (1), 1–26.

Bai, Y., Deng, X., Jiang, S., Zhang, Q., Wang, Z., 2018. Exploring the relationship between urbanization and urban eco-efficiency: Evidence from prefecture-level cities in China. Journal of Cleaner Production 195 1487–1496.

Chen, X., Zhao, H., Li, P., Yin, Z., 2006. Remote sensing image-based analysis of the relationship between urban heat island and land use/cover changes. Remote Sensing of Environment 104 (2), 133–146.

Ghayour, L., Neshat, A., Paryani, S., Shahabi, H., Shirzadi, A., Chen, W., et al., 2021. Performance evaluation of sentinel-2 and landsat 8 OLI data for land cover/use classification using a comparison between machine learning algorithms. Remote Sensing 13 (7), 1349.

Gogoi, P.P., Vinoj, V., Swain, D., Roberts, G., Dash, J., Tripathy, S., 2019. Land use and land cover change effect on surface temperature over Eastern India. Scientific reports 9 (1), 8859.

Gómez, C., White, J.C., Wulder, M.A., 2016. Optical remotely sensed time series data for land cover classification: A review. ISPRS Journal of photogrammetry and Remote Sensing 116 55–72.

Kipper, R., Fischer, M., Wiens, C., 2009. Cairo's informal areas, GTZ (Gesellschaft für Technische Zusammenarbeit), Cairo.

Lary, D.J., Alavi, A.H., Gandomi, A.H., Walker, A.L., 2016. Machine learning in geosciences and remote sensing. Geoscience Frontiers 7 (1), 3–10.

Pareeth, S., Karimi, P., Shafiei, M., De Fraiture, C., 2019. Mapping agricultural landuse patterns from time series of Landsat 8 using random forest based hierarchial approach. Remote Sensing 11 (5), 601.

Purevdorj, T.S., Tateishi, R., Ishiyama, T., Honda, Y., 1998. Relationships between percent vegetation cover and vegetation indices. International Journal of Remote Sensing 19 (18), 3519–3535.

Qu, L., Chen, Z., Li, M., Zhi, J., Wang, H., 2021. Accuracy improvements to pixel-based and object-based lulc classification with auxiliary datasets from Google Earth engine. Remote Sensing 13 (3), 453.

Rowland, C.S., Marston, C.G., Morton, R.D., O’Neil, A.W., 2020. Land Cover Change 1990-2015 (25m raster, GB).

Shih, H., Stow, D.A., Tsai, Y.H., 2019. Guidance on and comparison of machine learning classifiers for Landsat-based land cover and land use mapping. International Journal of Remote Sensing 40 (4), 1248–1274.

Solomon, B.D., 2023. Intergovernmental panel on climate change (IPCC), In: Dictionary of Ecological Economics, Anonymous Edward Elgar Publishing, pp. 302.

Tran, D.X., Pla, F., Latorre-Carmona, P., Myint, S.W., Caetano, M., Kieu, H.V., 2017. Characterizing the relationship between land use land cover change and land surface temperature. ISPRS Journal of Photogrammetry and Remote Sensing 124 119–132.

Wu, L., Zhu, X., Lawes, R., Dunkerley, D., Zhang, H., 2019. Comparison of machine learning algorithms for classification of LiDAR points for characterization of canola canopy structure. International Journal of Remote Sensing 40 (15), 5973–5991.

Xu, H., 2006. Modification of normalised difference water index (NDWI) to enhance open water features in remotely sensed imagery. International Journal of Remote Sensing 27 (14), 3025–3033.

Yang, L., Driscol, J., Sarigai, S., Wu, Q., Chen, H., Lippitt, C.D., 2022. Google Earth Engine and artificial intelligence (AI): a comprehensive review. Remote Sensing 14 (14), 3253.

You, H., Tang, X., Deng, W., Song, H., Wang, Y., Chen, J., 2022. A study on the difference of LULC classification results based on Landsat 8 and Landsat 9 data. Sustainability 14 (21), 13730.

Appendix

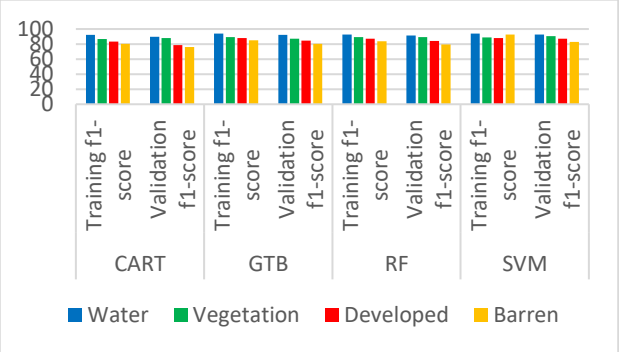

Figure 6. F1-score for the four classifiers.

Classifiers	Z-score	The probability of the first classifier performing better than the second
GTB vs CART	0.813987	58.43%
RF vs CART	0.857289	60.87%
SVM vs CART	1.43261	84.80%
RF vs GTB	0.043307	3.45%
SVM vs GTB	0.618743	46.39%
SVM vs RF	0.575438	43.50%

Table 4. Z-score results.

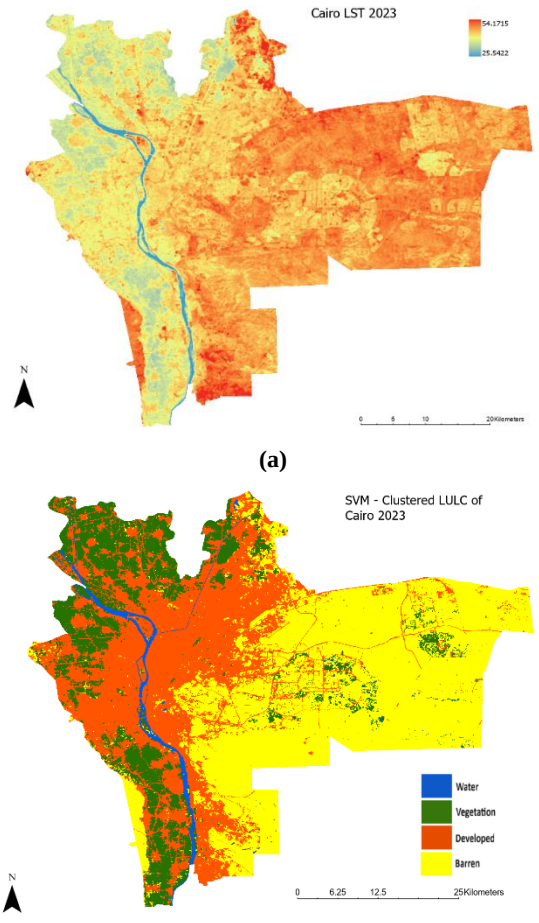

(a)

(b)

Figure 7. The 2023 LST map (a) in comparison to the LULC map (b) for Cairo.